The Astrophysical Journal Letters, 936:L21 (11pp), 2022 September 10 https://doi.org/10.3847/2041-8213/ac8c2c
© 2022. The Author(s). Published by the American Astronomical Society.
OPEN ACCESS

The Prolific Thermonuclear X-Ray Bursts from the Outburst of the Newly Discovered Millisecond Pulsar MAXI J1816–195 Observed by Insight-HXMT and NICER

Yu-Peng Chen[1], Shu Zhang[1], Long Ji[2], Shuang-Nan Zhang[1,3], Peng-Ju Wang[1,3], Ling-Da Kong[1,4], Zhi Chang[1], Jing-Qiang Peng[1,3], Qing-Cang Shui[1,3], Jian Li[5,6], Lian Tao[1], Ming-Yu Ge[1], and Jin-Lu Qu[1,3]
[1] Key Laboratory for Particle Astrophysics, Institute of High Energy Physics, Chinese Academy of Sciences, 19B Yuquan Road, Beijing 100049, People's Republic of China; chenyp@ihep.ac.cn, szhang@ihep.ac.cn
[2] School of Physics and Astronomy, Sun Yat-Sen University, Zhuhai, 519082, People's Republic of China; jilong@mail.sysu.edu.cn
[3] University of Chinese Academy of Sciences, Chinese Academy of Sciences, Beijing 100049, People's Republic of China
[4] Institut für Astronomie und Astrophysik, Kepler Center for Astro and Particle Physics, Eberhard Karls Universität, Sand 1, D-72076 Tübingen, Germany
[5] CAS Key Laboratory for Research in Galaxies and Cosmology, Department of Astronomy, University of Science and Technology of China, Hefei 230026, People's Republic of China
[6] School of Astronomy and Space Science, University of Science and Technology of China, Hefei 230026, People's Republic of China
Received 2022 July 26; revised 2022 August 19; accepted 2022 August 22; published 2022 September 9

Abstract

MAXI J1816–195 is a newly discovered accreting millisecond pulsar with prolific thermonuclear bursts, detected during its outburst in 2022 June by Insight-HXMT and NICER. During the outburst, Insight-HXMT detected 73 bursts in its peak and decay phase, serving as a prolific burst system found in the accreting millisecond pulsars. By analyzing one burst that was simultaneously detected by Insight-HXMT and NICER, we find a mild deviation from the conventional blackbody model. By stacking the Insight-HXMT light curves of 66 bursts that have similar profiles and intensities, a hard X-ray shortage is detected with a significance of 15.7σ in 30–100 keV. The shortage is about 30% of the persistent flux, which is low compared with other bursters. The shortage fraction is energy-dependent: larger in a higher energy band. These findings make the newly discovered millisecond MAXI J1816–195 a rather peculiar system compared with other millisecond pulsars and atoll bursters. In addition, based on the brightest burst, we derive an upper limit of the distance as 6.3 kpc, and therefore estimate the upper limit of the inner-disk radius of the accretion disk to be ∼40 km. Assuming the radius as the magnetospheric radius, the derived magnetic field strength is about 7.1×10^8 G.

Unified Astronomy Thesaurus concepts: X-ray bursters (1813)

1. Introduction

Accreting millisecond X-ray pulsars (hereafter AMXPs) are accretion-driven fast-spinning neutron stars (NSs) with periods shorter than 30 ms (for reviews, see Di Salvo 2022). It is thought that the accretion material stripped from the companion is channeled out of the accretion disk through the magnetic line and onto the NS's magnetic poles, which corresponds to the pulse formation process. As a subgroup of ∼130 low-mass X-ray binaries (LMXBs), since the discovery of the first AMXP (SAX J1808.4–3658) in 1998 by RXTE (Chakrabarty & Morgan 1998; Wijnands & van der Klis 1998), roughly two dozen of AMXPs have been discovered (Di Salvo 2022). For the X-ray emission during outbursts of AMXPs, the spectral characteristic resembles the hard states of NS LMXBs but with mild spectral evolution, composed of one or two blackbody-like components and an unsaturated Comptonization component with a corona temperature of tens of keV (Di Salvo 2022).

Half of the AMXPs exhibit thermonuclear bursts during their outbursts (Galloway et al. 2020). Thermonuclear bursts, also named type I X-ray bursts (hereafter bursts), are thermonuclear explosions triggered by unstable burning of accretion material accumulated on the NS surface. The bursting behavior of AMXPs also resembles other bursts in nonpulsation LMXBs. It manifests itself as a sudden increase (typically by a factor of 10 or greater) in the X-ray luminosity followed by an exponential decay (for reviews, see Lewin et al. 1993; Cumming 2004; Strohmayer & Bildsten 2006; Galloway et al. 2008).

Since a burst occurs at the NS surface, an interaction (Degenaar et al. 2018) between the burst emission and the neutron star environment should be detected. In the recent 10 yr, among thousands of observed bursts from the 118 bursters,[7] there are four major impacts observed on the accretion process by bursts, i.e., an enhancement at soft X-ray band, a shortage at hard X-ray band, a bump peaking at 20–40 keV, and/or discrete emission by reflection from an accretion disk (Ballantyne & Strohmayer 2004; in't Zand et al. 2013; Worpel et al. 2013; Keek et al. 2014), and a dip of the persistent emission due to the depleted accretion disk refilling itself (Bult et al. 2021).

For the enhancement at soft X-ray, it is thought that the entire persistent emission level (including disk and corona emission) becomes enhanced by a factor up to 10 (Worpel et al. 2013, 2015), alternatively, either the disk or the corona emission brightens (Koljonen et al. 2016; Kajava et al. 2017). These enhancements are observed in most bright bursts if the bursts are bright enough, e.g., in 4U 1636–536 (Zhao et al. 2022) and Aql X–1 (Güver et al. 2022).

The shortage during bursts in the hard X-ray of the continuum emission is reported on several bursters, i.e., IGR J17473–2721 (Chen et al. 2011a, 2012b), Aql X–1 (Maccarone & Coppi 2003; Chen et al. 2013), 4U 1636–536 (Ji et al. 2013; Chen et al. 2018; Güver et al. 2022a), GS 1826–238

Original content from this work may be used under the terms of the Creative Commons Attribution 4.0 licence. Any further distribution of this work must maintain attribution to the author(s) and the title of the work, journal citation and DOI.

[7] https://personal.sron.nl/~jeanz/bursterlist.html

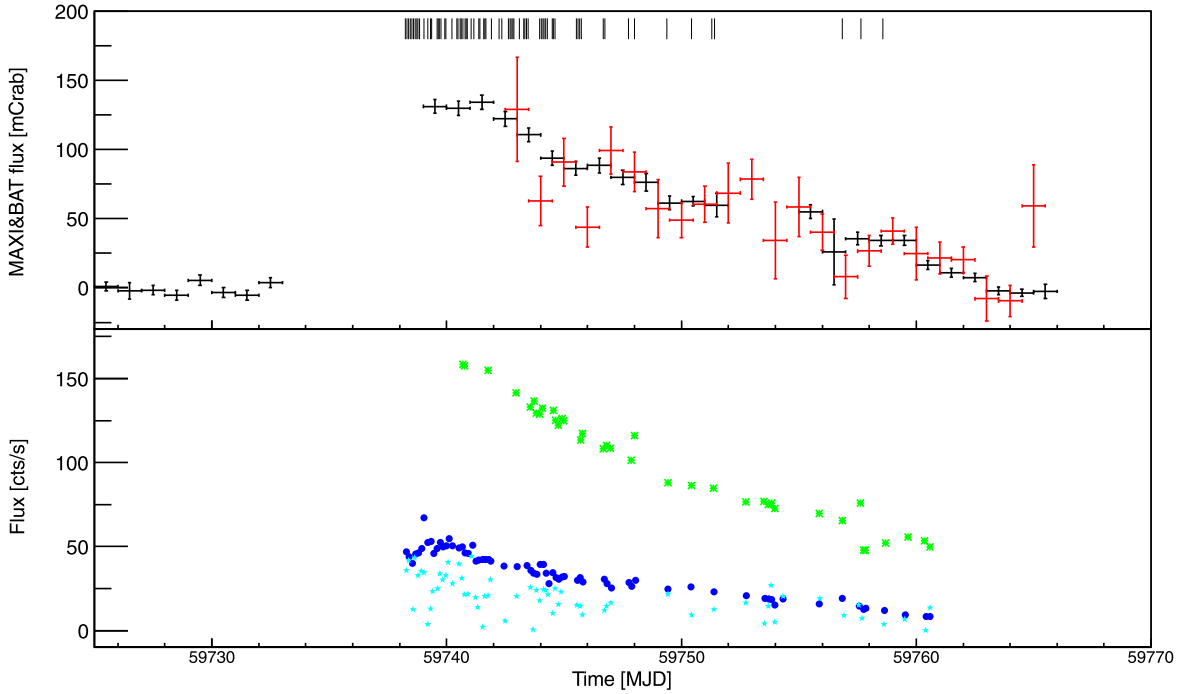

Figure 1. Top panel: daily light curves of MAXI J1816–195 by MAXI (black) and Swift/BAT (red) during the outbursts in 2022, in 2–20 keV and 15–50 keV, respectively. The 73 bursts are indicated by vertical lines. Bottom panel: light curves of MAXI J1816–195 by LE (green), ME (blue), and HE (teal), which are rebinned by one ObsID (∼10,000 s).

(Ji et al. 2014a; Sánchez-Fernández et al. 2020), KS 1731–260 (Ji et al. 2014b), 4U 1705–44 (Ji et al. 2014b), 4U 1728–34 (Kajava et al. 2017), and 4U 1724–30 (Kashyap & Chakraborty 2022), based on RXTE, INTEGRAL, Insight-HXMT, AstroSat, and NuSTAR observations.

MAXI J1816–195, an accretion-powered millisecond pulsar was discovered by MAXI in 2022 June (Negoro et al. 2022) with peak flux ∼100 mcrab, spin frequency 528 Hz (Bult et al. 2022a), and binary orbital period 17,402.27 s (Bult et al. 2022b). Its radio, infrared, and optical counterparts have been identified (Beauchamp et al. 2022; de Martino et al. 2022; Kennea et al. 2022). Insight-HXMT and NICER made dense observations on MAXI J1816–195 until its quiescent state, where 15 thermonuclear X-ray bursts have been detected by NICER (Bult et al. 2022c).

In this article, using all the Insight-HXMT observations and the first three observations (public until 2022 June 25) of NICER on MAXI J1816–195, the broadband energy light curves and spectra are studied for both the outburst and bursts. We derive the burst catalog detected by Insight-HXMT. To assess the burst influence on the persistent emission, we first analyze one burst that was simultaneously detected by Insight-HXMT and NICER, and then, by stacking tens of bursts detected by Insight-HXMT, the shortage in the hard X-ray band is given based on the broadband spectroscopy results. In the last section, we present our interpretation of these results.

2. Observations and Data Reduction

2.1. Insight-HXMT

The Hard X-ray Modulation Telescope (HXMT, also dubbed as Insight-HXMT; Zhang et al. 2020) excels in its broad energy band (1–250 keV) and large effective area in the hard X-ray energy band. It carries three collimated telescopes: the High Energy X-ray Telescope (HE; poshwich NaI/CsI, 20–250 keV, ∼5000 cm^2), the Medium Energy X-ray Telescope (ME; Si pin detector, 540 keV, 952 cm^2), and the Low Energy X-ray Telescope (LE; swept charge device detector, 1–12 keV, 384 cm^2). Under the quick read-out system of Insight-HXMT detectors, there is little pile-up effect at the burst peak. Insight-HXMT data analysis software (HXMTDAS) v2.05[8] is used to analyze the data.

As shown in Figure 1, starting from 2022 June 8 to 30, there are 77 observations ranging from P040427500101-20220608-01-01 to P040427502302-20220630-01-01 with a total observation time of 790 ks on MAXI J1816–195. These observations covered the peak and the decay phase of the outburst. All the observational data above are used in this work. Based on the standard pipeline of Insight-HXMT data analysis, the good-time-intervals (GTIs) of LE, ME, and HE are 28 ks, 181 ks, and 146 ks, respectively.

We note that the default GTI selection criteria of LE are very conservative because of the influence of light leaks. To obtain a complete sample of bursts, light curves are extracted without filtering GTIs. Burst-like fluctuations that may be caused by a sharp variation of the background, when the telescope passes the South Atlantic Anomaly, are excluded.

As shown in Table 2, 73 bursts are found in ME data; among them, 24 are found in LE data, and 70 are found in the HE light curves in 20–30 keV with a peak flux of ∼70 cts s^{-1} (except for the bright burst, ∼400 cts s^{-1} in the whole energy band of HE).

For each burst, we use the time of the ME flux peak as a reference (0 s in Figure 4) to produce light curves and spectra. Light curves of LE, ME, and HE are extracted with a time bin of 0.25 s. We extract time-resolved spectra of LE, ME, and HE with a bin size of 1 s starting from the onset of each burst (defined as the time 10 s before the burst peak). As a conventional procedure, the preburst emission (including the

[8] http://hxmtweb.ihep.ac.cn/

persistent emission and the instrumental background) is extracted, which is taken as the background when fitting spectra during bursts. In practice, for each burst, we define the time interval between 70 and 20 s before the burst peak as the time window of the preburst emission, i.e., [−70 s, −20 s].

The overlapped observations between Insight-HXMT and NICER are P040427500105-20220608-01-01 and 5533010101, respectively. Fortunately, these observations were located at the peak of the outburst. However, based on the recommended procedure of the Insight-HXMT data reduction guide v2.05[9], there is no good-time-interval of LE. We loosen the terms of screening criteria for LE data (from private advice from the Insight-HXMT team) with the value of the geomagnetic cutoff rigidity from >8 to >6; thus, we get a 120 s GTI of LE. The accompanying good-time-interval of ME and HE are 2300 s and 3100 s, which are used for joint spectra fitting of Insight-HXMT and NICER.

The other results, e.g., the persistent spectra, background, and net light curves are obtained following the recommended procedure of the Insight-HXMT data reduction guide, which are screened with the standard criterion included in Insight-HXMT pipelines: lepipeline, mepipeline, and hepipeline. The light curves are corrected for the dead time, e.g., the dead time reaches 5% at the peak of the burst for the HE light curves, which is close to the dead time on the blank sky observations.

For the persistent emission spectral fitting of LE, ME, and HE, the energy bands are chosen to be 2–7 keV and 8–30 keV, and 30–100 keV. The spectra are rebinned by the ftool ftgrouppha (Kaastra & Bleeker 2016) optimal binning algorithm with a minimum of 25 counts per grouped bin.

The LE background model works only in a certain temperature range. This leads to some uncertainties below 2 keV caused by the electronic noise when the temperature exceeds this range after the midyear of 2019. During a burst with a timescale of tens of seconds, the temperature fluctuation of LE is so small that it can be neglected. The resulting electronic noise of the preburst spectrum is the same as that of burst spectra. Therefore, the influence of the electronic noise can be canceled out when we take the preburst spectrum as the background of burst spectra. In this case, the energy band of LE can be extended to 1–10 keV.

The ME energy band used in burst spectral fitting is the same with the persistent emission analysis, i.e., 8–30 keV. The slices of burst spectra of LE and ME are rebinned by ftool grppha with a minimum of 10 counts per grouped bin, based on the limited photons of the burst slice spectra due to the short exposure time. We added a systematic uncertainty of 1% to the Insight-HXMT spectra to account for residual systematic uncertainties in the detector calibrations (Li et al. 2020).

2.2. NICER

Starting from 2022 June 7, NICER also performed dense observations on MAXI J1816–195. Three observation IDs (ObsIDs: 5202820101, 5202820102, 5533010101), from all the NICER public observations of MAXI J1816–195 until June 27, are used in this work. These observations have a GTI ∼15 ks and a count rate ∼600–800 cts s^{-1} in the 0.3–12 keV band. Among the three ObsIDs, one burst was detected in 5533010101, with a peak flux of 3018 cts s^{-1} . Fortunately, this burst is also the ninth burst detected by Insight-HXMT.

The NICER data are reduced using the pipeline tool nicerl2[10] in NICERDAS v7a with the standard NICER filtering and using ftool XSELECT to extract light curves and spectra. The background is estimated using the tool nibackgen3C50 (Remillard et al. 2022). The focal plane module number 14 and 34 are removed from the analysis because of increased detector noise. The response matrix files and ancillary response files are generated with the ftool nicerrmf and nicerarf. The spectra are rebinned by the ftool ftgrouppha (Kaastra & Bleeker 2016) optimal binning algorithm with a minimum of 25 counts per grouped bin.

For the burst detected by NICER, we use the reference time of the ninth burst of Insight-HXMT and divide the burst into intervals of 1 s after the burst onset, and extract the spectra. As a conventional procedure, the preburst emission (including the persistent emission and the instrumental background) is extracted as the background when fitting burst spectra, using the same time interval dealing with the bursts detected by Insight-HXMT: [−70 s, −20 s]. The spectral slices of bursts by NICER are rebinned by ftool grppha with a minimum of 20 counts per grouped bin.

The tbabs model with Wilm abundances accounts for the interstellar medium absorption in the spectral model (Wilms et al. 2000). To erase the residuals in the spectral fitting of the persistent spectra <1 keV, which are caused by the NICER instrument and the unmodeled background, the channels <1 keV are ignored. By the same token, the energy band is extended to 0.4–10 keV during burst spectral fitting.

The resulting spectra were analyzed using XSPEC (Arnaud 1996) version 12.11.1. We added a systematic uncertainty of 1% to the NICER spectrum

3. Analysis and Results

3.1. Fitting the Joint Insight-HXMT/NICER Spectra of Persistent Emission

We fit the joint NICER and Insight-HXMT (LE and ME) spectrum with an absorbed convolution thermal Comptonization model (with an input seed photon spectra diskbb), available as thcomp (a more accurate version of nthcomp; Zdziarski et al. 2020) in XSPEC, which is described by the optical depth τ, electron temperature kT_e, and scattered/covering fraction f_{sc}.

The hydrogen column (tbabs in XSPEC) accounts for both the line-of-sight column density, as well as any intrinsic absorption near the source. The seed photons are in the shape of diskbb since the thcomp model is a convolution model, and a fraction of Comptonization photons is also given in the model.

Normalization constants are included during fittings to take into account the intercalibrations of the instruments. We keep the normalization factor of the NICER data with respect to the LE, ME, and HE data to unity. To ease the residuals around 6.4 keV, a Gaussian emission line is added and fixed at 6.4 keV, corresponding to the iron emission line reflected from the disk.

Using the model above, we find an acceptable fit: reduced $\chi_\upsilon = 1.13$ (degress of freedom (dof) 192; Figure 2 and Table 1), with the inner-disk radius R_{diskbb}, and temperature kT_{in} found to be $\sim 39.6 \pm 5.1$ km (with a distance 6.3 kpc and an inclination angle 0°) and 0.48 ± 0.01 keV, respectively. The

[9] http://hxmtweb.ihep.ac.cn/SoftDoc.jhtml

[10] https://heasarc.gsfc.nasa.gov/docs/nicer/nicer_analysis.html

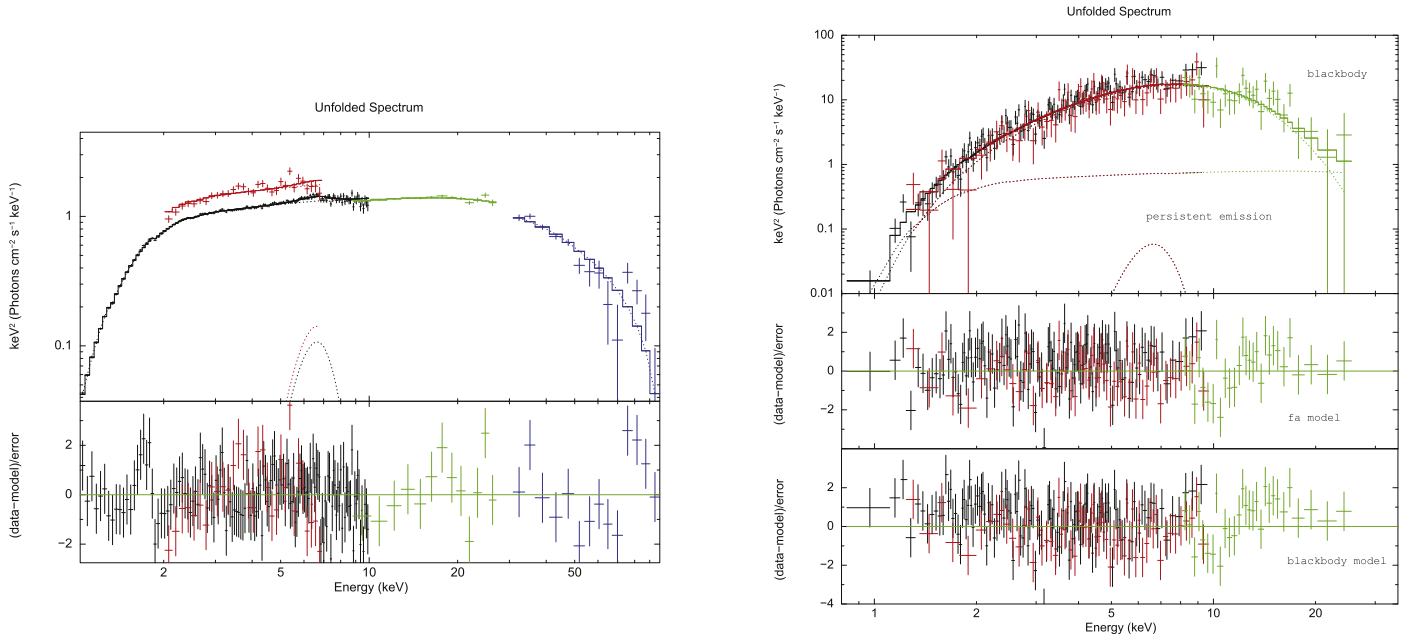

Figure 2. Left panel: simultaneous broadband energy spectrum of MAXI J1816–195 as observed from NICER (black), Insight-HXMT/LE (red), Insight-HXMT/ME (green), and Insight-HXMT/HE (blue); the best-fitting model consists of an absorbed convolution thermal Comptonization model (with an input seed photon spectrum diskbb) and an absorbed Gaussian emission line fixed at 6.4 keV. Right panel: the spectral fitting results by NICER (black), Insight-HXMT/LE (red), and Insight-HXMT/ME (green) when the burst reached its peak flux with the f_a model (top). The blackbody model and the enhancement of the persistent emission are labeled. The two panels below: residuals of spectral fitting results by the f_a model (middle) and an absorbed blackbody (bottom).

Table 1
The Results of the Spectral Fitting of the Joint LE, ME, HE, and NICER Spectrum in the 1–100 keV Range with cons*tbabs*(thcomp*diskbb+Gauss)

$N_{\rm H}$ (10^{22} cm^{-2})	τ	$kT_{\rm e}$ (keV)	$f_{\rm sc}$ (keV)	$kT_{\rm in}$	$N_{\rm diskbb}$ (10^2)	$E_{\rm Fe}$ (keV)	$\sigma_{\rm Fe}$ (keV)	$A_{\rm Fe}$ (10^{-3} cts cm^2 s^{-1})	χ^2_ν	$F_{\rm bol}$ (10^{-8} erg cm^2 s^{-1})
$2.37^{+0.02}_{-0.03}$	$5.41^{+0.25}_{-0.07}$	$10.8^{+0.6}_{-0.2}$	$0.52^{+0.02}_{-0.01}$	$0.48^{+0.01}_{-0.01}$	$39.5^{+5.1}_{-5.1}$	6.4 (fxd)	$0.86^{+0.15}_{-0.14}$	$5.4^{+0.9}_{-1.1}$	217/192	$1.11^{+0.01}_{-0.01}$

thcomp parameters of the electron temperature $kT_{\rm e}$, optical depth τ, and scattered/covering fraction $f_{\rm sc}$ are $10.8^{+0.6}_{-0.2}$ keV, $5.41^{+0.25}_{-0.07}$, and 0.48 ± 0.01, respectively. The derived hydrogen column density $N_{\rm H}$ is $2.37^{+0.02}_{-0.03} \times 10^{22}$ cm^{-2}.

The constants of LE, ME, and HE are $1.33^{+0.12}_{-0.15}$, 0.97 ± 0.02, and 0.81 ± 0.04, respectively. The inferred bolometric flux in 0.01–1000 keV is $1.11 \pm 0.01 \times 10^{-8}$ erg cm^{-2} s^{-1}, corresponding to $28.9\% L_{\rm Ledd}$ at a distance of 6.3 kpc and $L_{\rm Ledd} = 1.8 \times 10^{38}$ erg s^{-1}.

The other scenario, i.e., substituting the diskbb component by a blackbody component in the aforementioned convolution model, is also attempted. Taking this approach, spectral fits yield roughly the same thcomp parameters and reduced $\chi_\upsilon = 1.12$ (the same dof). However, the derived blackbody radius is 86 ± 10 km, which is far greater than the NS radius, although it is an upper limit considering the distance used is an upper limit. Suppose the derived blackbody radius was comparable with the radius of the NS ~10 km, the distance adopted should be ~0.8 kpc, which is unlikely to occur.

3.2. Fitting the Joint Insight-HXMT/NICER Spectra of Burst Emission

We follow the classical approach to X-ray burst spectroscopy by subtracting the persistent spectrum and fitting the net spectrum with an absorbed blackbody and a fixed hydrogen column density derived from the fitting result of persistent emission. As shown in Figure 2 and Figure 3, such a spectral model generally results in an acceptable goodness of fit, with a mean reduced $\chi^2_\upsilon \sim 0.8$–1.2 (dof 70–200). The profiles flux, temperature, and radius are characteristic of bursts: a flux with fast rising, exponential decaying, and spectral softening during decay. The temperature and radius reach a maximum value of ~2 keV and ~11 km at the burst peak.

The f_a model is also used to fit the burst spectra. Following Worpel et al. (2013) we then include an additional component for fitting the variable persistent emission. We assume that during the burst the spectral shape of the persistent emission is unchanged, and only its normalization (known as a f_a factor) is changeable. We compare the above two models using the F-test. In most cases, the f_a model does not apparently improve the fits with a p-value $>3 \times 10^{-3}$ except the spectrum when the burst reaches its peak flux. For the spectrum when the burst reaches its peak flux, the f_a factor reaches a maximum 0.54 ± 0.11[11], accompanying with the change of the temperature and the radius of the blackbody within a variation of ~10%. As shown in Figure 2, at this data point, the f_a improves the fits with a p-value 2.3×10^{-5}.

3.3. Fitting the Insight-HXMT Spectra of Burst Emission

The same procedure on all bursts is carried out to fit the burst spectra detected by Insight-HXMT. As shown in Table 2, the

[11] Please note that the definition of f_a in our paper is not the same as the traditional one by Worpel et al. (2013). Instead, our definition of $f_a = 0$ indicates that there is no enhancement or deficit of the persistent emission during the burst.

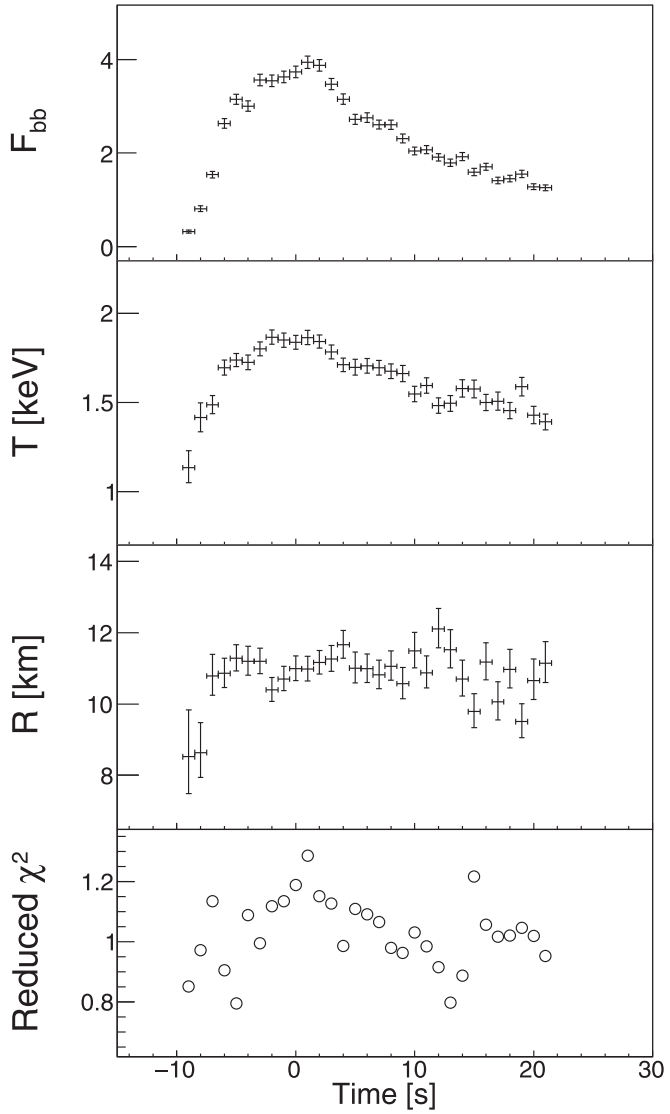

Figure 3. Spectral fitting result of burst nine with time bin 1 s with an absorbed blackbody (black), including the time evolution of the blackbody bolometric flux $F_{\rm bb}$, the temperature $kT_{\rm bb}$, the observed radius R of NS surface at 6.3 kpc, the goodness of fit χ^2_ν. The bolometric flux of the blackbody model $F_{\rm bb}$ is in units of 10^{-8} erg cm^{-2} s^{-1}.

burst unabsorbed bolometric peak flux $F_{\rm p}$, burst fluence $E_{\rm b}$, and burst duration $\tau = E_{\rm b}/F_{\rm pk}$, are given.

The brightest burst is the last burst number 73, with a maximum peak flux $8.03^{+0.40}_{-0.39} \times 10^{-8}$ erg cm^{-2} s^{-1}. The burst did not show photospheric radius expansion; assuming the empirical Eddington luminosity of 3.8×10^{38} erg s^{-1} (Kuulkers et al. 2003), we derive an upper limit on the source distance of 6.3 kpc.

Based on the bursts time interval ~1.15 hr, the ratio α of the integrated persistent flux to the burst fluence is ~45 (a detailed study on the burst statistical behaviors will be reported elsewhere by P.-J. Wang et al. 2022, in preparation).

3.4. Stacked Light Curves/Spectra of Bursts by Insight-HXMT

In the HE light curves above 30 keV, we notice there is no significant flux deviation from the persistent emission during the burst. It is caused by the vast majority of the thermal emission of an X-ray burst outside the HE energy range (>30 keV). The same as our previous procedures (Chen et al. 2013), the burst light curves are stacked to improve the statistics.

Table 2 shows that most bursts have a peak flux ~4×10^{-8} erg cm^2 s^{-1} and a duration ~20 s, except the last seven bursts. Thus, we choose the first 66 bursts to stack since after that the persistent emission in the hard X-ray band is <100 mcrab and the latter bursts have a different profile. Our forthcoming publication will give other features, e.g., burst profiles, intervals, and relation with persistent emission. With respect to the burst peak time as a reference time, the light curves of the 66 bursts are stacked and averaged in each time bin, respectively.

As shown in Figure 4, accompanying the burst rise detected by LE and ME, there is a flux dropping in the HE light curves. Following the decay of the bursts, the HE flux restores to the preburst level. Considering the preburst emission of ~337 cts s^{-1} (including ~40 cts s^{-1} persistent emission and ~297 cts s^{-1} background emission), the HE decrement reaches a maximum of ~12 cts s^{-1} at the burst peak, which amounts to ~30% of the whole persistent flux in 30–100 keV. The average deficit from −5 to 45 s (burst peak time as 0 s) is -7.59 ± 0.33 cts s^{-1} .

A cross-correlation analysis is performed between LE and HE light curves with a bin size of 0.25 s (for details, see Chen et al. 2012b). The minimum of the cross-correlation function appears at ~1 s, which indicates that the hard X-ray deficit lags the burst emission with ~1 s.

To estimate the deficit significance, another approach based on the stacked spectra is carried out. First, we extract each burst with an exposure time of 50 s, i.e., the interval of 5 s before the burst peak to 45 s after the burst peak. Then, ftool addspec is used to combine the burst spectrum. All the preburst spectra with the same exposure time are also stacked.

Based on the stacked spectra of burst and preburst emission, we get the count numbers for the burst ($N_{\rm b} = 971{,}431$ counts) and the preburst ($N_{\rm pre} = 993{,}402$ counts) with a same exposure time in 30–100 keV. Assuming the count numbers follow a Gaussian distribution, the significance of this deficit in 30–100 keV is estimated at $(N_{\rm pre} - N_{\rm b})/\sqrt{N_{\rm pre} + N_{\rm b}} = 15.7\sigma$.

To further estimate the variation of the deficit with the energy, two spectra are used as inputs for estimation, i.e., the detected spectrum of the burst (the middle panel of Figure 5), and the spectrum of persistent emission (the top panel of Figure 5). The first spectrum is given in the paragraph above. The last spectrum is derived by stacking the spectra of the persistent emission.

The fraction of the deficit is the ratio of the two spectra above, i.e., the value of the deficit divided by the persistent emission. As shown in Figure 5, for the fraction of the deficit, there is a variability trend with energy: it increases with energy.

4. Discussion

This paper analyzes the broadband X-ray light curves and spectra for the persistent emission and thermonuclear bursts acquired during the 2022 outburst of the AMXP MAXI J1816–195 observed by NICER and Insight-HXMT.

The observations of Insight-HXMT and NICER were performed simultaneously at the peak of the outburst on 2022 June 8. This way, we obtained a broadband (from 1 to 100 keV) source spectrum. We find clear evidence of a broad iron line that we interpret as produced by reflection from the inner accretion disk. However, no significant reflection bump around

Table 2
The Bursts Detected by Insight/HXMT in 2022 Outburst of MAXI J1816–195

No.	ObsID	Time (MJD)	F_p (10^{-8} erg cm^{-2} s^{-1})	E_b (10^{-8} erg cm^{-2})	τ (s)
1	P040427500101-20220608-01-01	59738.23551	$3.17^{+0.47}_{-0.41}$	$61.9^{+2.6}_{-2.5}$	$19.5^{+3.0}_{-2.6}$
2	P040427500101-20220608-01-01	59738.31022	$3.02^{+0.41}_{-0.34}$	$59.8^{+2.3}_{-2.2}$	$19.8^{+2.8}_{-2.4}$
3	P040427500102-20220608-01-01	59738.38172	$3.02^{+0.47}_{-0.39}$	$73.6^{+3.1}_{-2.9}$	$24.3^{+3.9}_{-3.3}$
4	P040427500102-20220608-01-01	59738.45275	$3.45^{+0.43}_{-0.37}$	$60.5^{+2.6}_{-2.4}$	$17.5^{+2.3}_{-2.0}$
5	P040427500103-20220608-01-01	59738.52387	$3.52^{+0.52}_{-0.44}$	$70.8^{+2.8}_{-2.6}$	$20.1^{+3.1}_{-2.6}$
6	P040427500103-20220608-01-01	59738.59306	$3.43^{+0.54}_{-0.45}$	$71.2^{+3.1}_{-2.9}$	$20.7^{+3.4}_{-2.9}$
7	P040427500104-20220608-01-01	59738.66072	$4.14^{+0.59}_{-0.50}$	$70.0^{+3.3}_{-3.1}$	$16.9^{+2.5}_{-2.2}$
8	P040427500104-20220608-01-01	59738.72614	$3.60^{+0.16}_{-0.16}$	$88.1^{+1.0}_{-1.0}$	$24.5^{+1.1}_{-1.1}$
9[a]	P040427500105-20220608-01-01	59738.78847	$3.54^{+0.17}_{-0.17}$	$96.6^{+1.2}_{-1.1}$	$27.3^{+1.3}_{-1.3}$
10	P040427500105-20220608-01-01	59738.85032	$4.27^{+0.63}_{-0.53}$	$75.1^{+3.3}_{-3.1}$	$17.6^{+2.7}_{-2.3}$
11	P040427500107-20220608-01-01	59739.02920	$4.19^{+0.71}_{-0.58}$	$70.5^{+2.6}_{-2.4}$	$16.8^{+2.9}_{-2.4}$
12	P040427500201-20220609-01-01	59739.19766	$3.40^{+0.47}_{-0.41}$	$76.7^{+3.2}_{-3.0}$	$22.6^{+3.3}_{-2.9}$
13	P040427500202-20220609-01-01	59739.30639	$3.00^{+0.36}_{-0.32}$	$77.9^{+3.2}_{-3.0}$	$25.9^{+3.3}_{-2.9}$
14	P040427500202-20220609-01-01	59739.36110	$3.44^{+0.49}_{-0.42}$	$73.1^{+2.9}_{-2.7}$	$21.2^{+3.1}_{-2.7}$
15	P040427500204-20220609-01-01	59739.58436	$3.60^{+0.68}_{-0.55}$	$80.3^{+3.3}_{-3.1}$	$22.3^{+4.3}_{-3.5}$
16	P040427500204-20220609-01-01	59739.64061	$3.38^{+0.48}_{-0.40}$	$81.6^{+3.4}_{-3.2}$	$24.1^{+3.6}_{-3.0}$
17	P040427500205-20220609-01-01	59739.69725	$2.90^{+0.35}_{-0.31}$	$72.2^{+2.9}_{-2.7}$	$24.9^{+3.2}_{-2.8}$
18	P040427500205-20220609-01-01	59739.75401	$3.82^{+0.58}_{-0.49}$	$74.6^{+3.0}_{-2.9}$	$19.5^{+3.1}_{-2.6}$
19	P040427500206-20220609-01-01	59739.92397	$3.43^{+0.45}_{-0.39}$	$77.8^{+3.1}_{-3.0}$	$22.7^{+3.1}_{-2.7}$
20	P040427500207-20220609-01-01	59739.97869	$3.58^{+0.17}_{-0.17}$	$100.9^{+1.1}_{-1.1}$	$28.2^{+1.3}_{-1.3}$
21	P040427500302-20220610-01-01	59740.23140	$2.74^{+0.33}_{-0.29}$	$73.0^{+2.9}_{-2.8}$	$26.7^{+3.4}_{-3.0}$
22	P040427500303-20220610-01-01	59740.43116	$3.42^{+0.64}_{-0.50}$	$74.2^{+3.2}_{-3.0}$	$21.7^{+4.2}_{-3.3}$
23	P040427500304-20220610-01-01	59740.48185	$3.19^{+0.48}_{-0.41}$	$70.2^{+2.9}_{-2.7}$	$22.0^{+3.5}_{-2.9}$

Table 2
(Continued)

No.	ObsID	Time (MJD)	F_p (10^{-8} erg cm^{-2} s^{-1})	E_b (10^{-8} erg cm^{-2})	τ (s)
24	P040427500304-20220610-01-01	59740.58205	$3.28^{+0.16}_{-0.16}$	$82.9^{+1.1}_{-1.1}$	$25.3^{+1.2}_{-1.2}$
25	P040427500305-20220610-01-01	59740.62985	$2.87^{+0.66}_{-0.50}$	$61.5^{+3.0}_{-2.8}$	$21.5^{+5.0}_{-3.9}$
26	P040427500305-20220610-01-01	59740.68092	$3.20^{+0.45}_{-0.38}$	$75.0^{+3.1}_{-2.9}$	$23.4^{+3.4}_{-2.9}$
27	P040427500306-20220610-01-01	59740.78507	$2.60^{+0.36}_{-0.30}$	$68.0^{+2.8}_{-2.6}$	$26.1^{+3.7}_{-3.2}$
28	P040427500306-20220610-01-01	59740.83742	$3.42^{+0.17}_{-0.17}$	$94.5^{+1.1}_{-1.1}$	$27.6^{+1.4}_{-1.4}$
29	P040427500307-20220610-01-01	59740.88945	$3.58^{+0.67}_{-0.55}$	$75.1^{+3.4}_{-3.2}$	$21.0^{+4.0}_{-3.3}$
30	P040427500401-20220611-01-01	59741.04474	$3.54^{+0.16}_{-0.16}$	$92.8^{+1.1}_{-1.1}$	$26.2^{+1.2}_{-1.2}$
31	P040427500401-20220611-01-01	59741.14988	$3.35^{+0.47}_{-0.40}$	$77.9^{+3.1}_{-2.9}$	$23.2^{+3.4}_{-2.9}$
32	P040427500403-20220611-01-01	59741.36075	$2.68^{+0.29}_{-0.26}$	$62.6^{+2.5}_{-2.3}$	$23.3^{+2.6}_{-2.4}$
33	P040427500403-20220611-01-01	59741.41406	$3.23^{+0.39}_{-0.35}$	$74.8^{+3.1}_{-2.9}$	$23.1^{+3.0}_{-2.6}$
34	P040427500404-20220611-01-01	59741.57413	$3.41^{+0.16}_{-0.16}$	$90.1^{+1.1}_{-1.1}$	$26.4^{+1.3}_{-1.3}$
35	P040427500405-20220611-01-01	59741.62791	$2.78^{+0.39}_{-0.33}$	$69.6^{+2.8}_{-2.7}$	$25.0^{+3.6}_{-3.1}$
36	P040427500405-20220611-01-01	59741.68257	$3.13^{+0.62}_{-0.47}$	$75.4^{+3.1}_{-3.0}$	$24.1^{+4.9}_{-3.7}$
37	P040427500407-20220611-01-01	59741.90167	$3.61^{+0.16}_{-0.16}$	$84.1^{+0.9}_{-0.9}$	$23.3^{+1.1}_{-1.1}$
38	P040427500501-20220612-01-01	59742.23829	$4.22^{+0.72}_{-0.59}$	$74.8^{+4.2}_{-3.9}$	$17.7^{+3.2}_{-2.6}$
39	P040427500501-20220612-01-01	59742.35230	$3.55^{+0.38}_{-0.34}$	$60.1^{+2.3}_{-2.2}$	$16.9^{+1.9}_{-1.7}$
40	P040427500503-20220612-01-01	59742.63528	$3.73^{+0.16}_{-0.16}$	$98.4^{+1.1}_{-1.0}$	$26.4^{+1.2}_{-1.2}$
41	P040427500504-20220612-01-01	59742.69325	$3.49^{+0.16}_{-0.16}$	$84.3^{+0.9}_{-0.9}$	$24.1^{+1.1}_{-1.1}$
42	P040427500504-20220612-01-01	59742.75051	$3.55^{+0.66}_{-0.53}$	$70.1^{+2.9}_{-2.8}$	$19.7^{+3.8}_{-3.1}$
43	P040427500505-20220612-01-01	59742.80863	$4.22^{+0.54}_{-0.47}$	$72.3^{+2.5}_{-2.4}$	$17.1^{+2.3}_{-2.0}$
44	P040427500505-20220612-01-01	59742.86578	$3.65^{+0.54}_{-0.46}$	$75.3^{+2.9}_{-2.8}$	$20.6^{+3.2}_{-2.7}$
45	P040427500601-20220613-01-01	59743.09808	$3.42^{+0.16}_{-0.16}$	$95.3^{+1.0}_{-1.0}$	$27.9^{+1.3}_{-1.3}$
46	P040427500602-20220613-01-01	59743.27835	$3.66^{+0.50}_{-0.43}$	$75.8^{+2.9}_{-2.8}$	$20.7^{+2.9}_{-2.5}$

Table 2
(Continued)

No.	ObsID	Time (MJD)	F_p (10^{-8} erg cm^{-2} s^{-1})	E_b (10^{-8} erg cm^{-2})	τ (s)
47	P040427500602-20220613-01-01	59743.33933	$3.53^{+0.58}_{-0.48}$	$77.7^{+3.3}_{-3.1}$	$22.0^{+3.7}_{-3.1}$
48	P040427500603-20220613-01-01	59743.40185	$3.26^{+0.42}_{-0.36}$	$75.5^{+2.9}_{-2.8}$	$23.2^{+3.1}_{-2.7}$
49	P040427500603-20220613-01-01	59743.46334	$3.26^{+0.48}_{-0.40}$	$63.4^{+2.2}_{-2.1}$	$19.5^{+3.0}_{-2.5}$
50	P040427500607-20220613-01-01	59743.96283	$3.45^{+0.48}_{-0.41}$	$77.4^{+2.9}_{-2.7}$	$22.4^{+3.2}_{-2.8}$
51	P040427500607-20220613-01-01	59744.02764	$3.41^{+0.50}_{-0.42}$	$79.1^{+3.0}_{-2.8}$	$23.2^{+3.5}_{-3.0}$
52	P040427500608-20220614-02-01	59744.09221	$3.87^{+0.16}_{-0.16}$	$101.6^{+1.0}_{-1.0}$	$26.2^{+1.1}_{-1.1}$
53	P040427500608-20220614-02-01	59744.15880	$3.71^{+0.16}_{-0.16}$	$97.5^{+1.0}_{-1.0}$	$26.3^{+1.2}_{-1.2}$
54	P040427500609-20220614-02-01	59744.22394	$3.77^{+0.17}_{-0.17}$	$89.5^{+1.0}_{-1.0}$	$23.7^{+1.1}_{-1.1}$
55	P040427500609-20220614-02-01	59744.28849	$3.69^{+0.61}_{-0.50}$	$112.6^{+1.8}_{-1.8}$	$30.6^{+5.1}_{-4.1}$
56	P040427500611-20220614-02-01	59744.48935	$4.00^{+0.16}_{-0.16}$	$111.1^{+1.0}_{-1.0}$	$27.8^{+1.1}_{-1.1}$
57	P040427500611-20220614-02-01	59744.55683	$3.34^{+0.48}_{-0.41}$	$76.3^{+3.0}_{-2.8}$	$22.9^{+3.4}_{-2.9}$
58	P040427500612-20220614-02-01	59744.62540	$3.30^{+0.53}_{-0.44}$	$76.9^{+3.4}_{-3.2}$	$23.3^{+3.9}_{-3.2}$
59	P040427500701-20220615-01-01	59745.52358	$3.57^{+0.48}_{-0.42}$	$79.6^{+3.1}_{-2.9}$	$22.3^{+3.1}_{-2.7}$
60	P040427500701-20220615-01-01	59745.59710	$3.67^{+0.52}_{-0.44}$	$81.7^{+3.6}_{-3.4}$	$22.2^{+3.3}_{-2.8}$
61	P040427500702-20220615-01-01	59745.67103	$4.19^{+0.64}_{-0.53}$	$75.2^{+3.1}_{-3.0}$	$17.9^{+2.8}_{-2.4}$
62	P040427500702-20220615-01-01	59745.74569	$3.96^{+0.16}_{-0.16}$	$97.0^{+1.0}_{-1.0}$	$24.5^{+1.0}_{-1.0}$
63	P040427500801-20220616-01-01	59746.66017	$3.25^{+0.53}_{-0.45}$	$65.3^{+2.9}_{-2.7}$	$20.1^{+3.4}_{-2.9}$
64	P040427500801-20220616-01-01	59746.74048	$3.85^{+0.16}_{-0.16}$	$98.3^{+1.0}_{-1.0}$	$25.6^{+1.1}_{-1.1}$
65	P040427500901-20220617-01-01	59747.73360	$3.58^{+0.46}_{-0.39}$	$79.7^{+3.1}_{-3.0}$	$22.3^{+3.0}_{-2.6}$
66	P040427500903-20220617-01-01	59747.99203	$3.94^{+0.16}_{-0.16}$	$98.9^{+1.0}_{-1.0}$	$25.1^{+1.1}_{-1.1}$
67	P040427501101-20220619-01-01	59749.36886	$4.24^{+0.52}_{-0.46}$	$66.0^{+2.5}_{-2.4}$	$15.6^{+2.0}_{-1.8}$
68	P040427501201-20220620-01-01	59750.41864	$3.92^{+0.50}_{-0.43}$	$63.3^{+2.6}_{-2.4}$	$16.2^{+2.2}_{-1.9}$
69	P040427501301-20220621-01-01	59751.30502	$4.08^{+0.17}_{-0.17}$	$78.1^{+0.9}_{-0.9}$	$19.1^{+0.8}_{-0.8}$

Table 2
(Continued)

No.	ObsID	Time (MJD)	F_p (10^{-8} erg cm^{-2} s^{-1})	E_b (10^{-8} erg cm^{-2})	τ (s)
70	P040427501301-20220621-01-01	59751.41726	$3.71^{+0.46}_{-0.40}$	$63.5^{+2.8}_{-2.6}$	$17.1^{+2.3}_{-2.0}$
71	P040427501901-20220626-01-01	59756.85801	$6.60^{+0.22}_{-0.22}$	$87.7^{+0.9}_{-0.9}$	$13.3^{+0.5}_{-0.5}$
72	P040427502001-20220627-01-01	59757.65185	$4.84^{+0.42}_{-0.38}$	$52.8^{+1.9}_{-1.8}$	$10.9^{+1.0}_{-0.9}$
73	P040427502101-20220628-01-01	59758.58367	$8.03^{+0.40}_{-0.39}$	$82.6^{+1.5}_{-1.5}$	$10.3^{+0.5}_{-0.5}$

Note.
[a] The burst is detected simultaneously by NICER and Insight-HXMT.

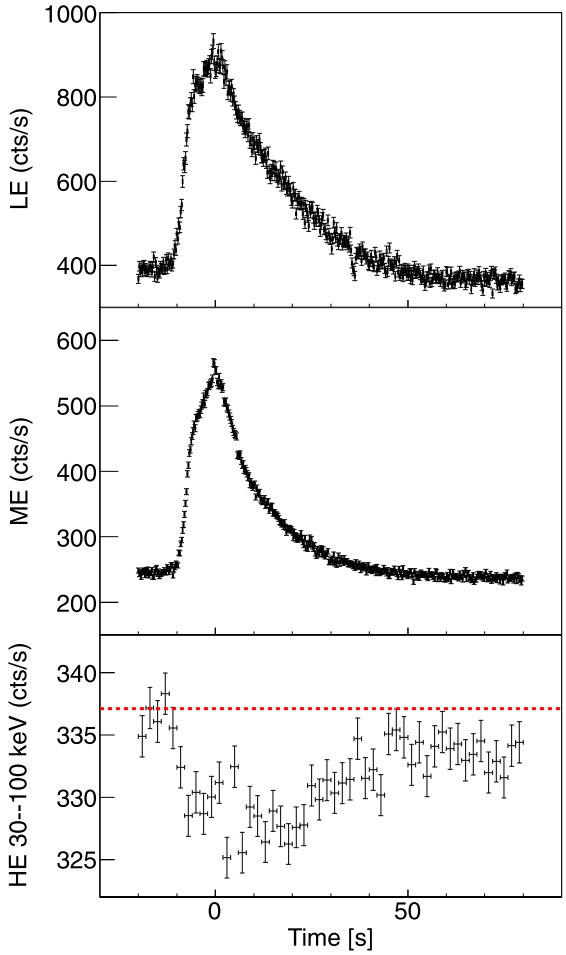

Figure 4. The stacked light curves of LE (top), ME (middle), and HE (bottom) of the burst in 1–10 keV, 8–30 keV, and 30–100 keV, respectively. The time bin for LE and ME is 0.25 s; for the HE it is 2 s. The red line in the bottom panel indicates the preburst emission (persistent emission and background) in the HE detectors. There is 1 s data gap around $T = 35$ in the LE light curve of burst nine, which causes a dip around $T = 35$. For other bursts, for LE, ME, and HE, there is no such gap observed.

30 keV was observed. This might be due to the high background level of ME and HE in this energy band.

The outburst's peak bolometric luminosity is roughly $< 30\%L_{\rm Edd}$ under an upper limit of the distance 6.3 kpc. Based on the normalization of the disk emission derived from spectral fitting,

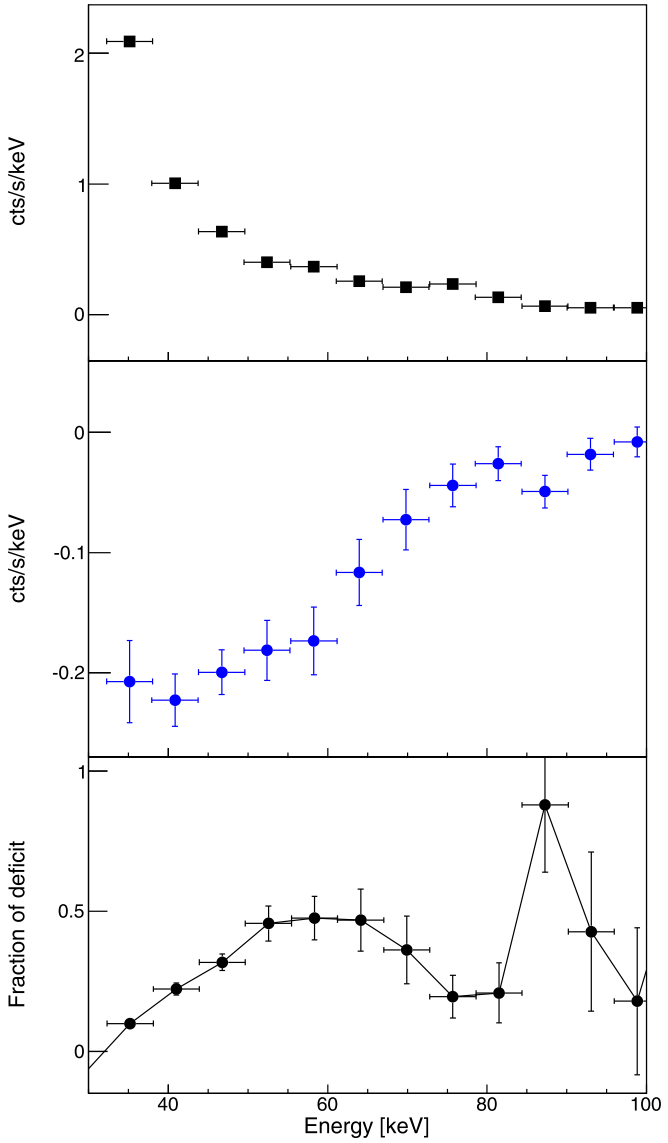

Figure 5. Top panel: the spectrum of the persistent emission by HE. Middle panel: the detected spectrum of the bursts. Bottom panel: deficit fraction VS energy during the bursts detected by HE.

the estimated inner-disk radius is ∼40 km, assuming an inclination angle of zero (face-on scenario) and a distance of 6.3 kpc. The inner-disk radius of AMXPs is widely used to derive the magnetic field of the NS, although there is a large systematic uncertainty. Taking the Alfvén radius as the magnetospheric radius (Ghosh & Lamb 1978; Wang 1997; Burderi et al. 1998), the magnetic field is estimated as 7.1×10^8 Gauss (Mestel 1968 or Equation (4) from Di Salvo 2022). The corotation radius at which the angular velocity of Keplerian motion matches that of the NS is estimated at 25.3 km for MAXI J1816–195. Considering the inclination angle and distance uncertainties, the two radii above are consistent.

We notice that the ratio α between the fluxes of the persistent and bursts emission is ∼45, which is consistent with the value derived from 15 bursts detected by NICER (Bult et al. 2022c). Accompanying most of the burst durations $\tau > 10$ s and the burst occurred persistent emission $<30\% L_{\rm Edd}$, it indicates that most of these bursts occurred when the helium ignites unstably in a hydrogen-rich environment, i.e., a mixed hydrogen/helium burning since the hydrogen is accreted faster than it can be consumed by steady burning. For the last several bursts, including the bright one, the persistent emission decayed to one-third of its peak flux $<10\% L_{\rm Edd}$, and these bursts behave with a shorter duration of ∼10 s and a brighter peak flux, which indicates a change of material in the burning: a pure helium burning instead of a mixed hydrogen/helium burning because of the hydrogen burning stably into the helium between bursts under a lower accretion rate than that of the preceding bursts. These findings are consistent with the canonical theoretical ignition models of thermonuclear bursts (e.g., Galloway et al. 2008).

For the persistent emission, we notice that the spectrum could be well fitted with a convolution thermal Comptonization model with input seed photons from the accretion disk, and the thermal emission from the NS surface is not observed. In particular, the scattered/covering fraction of the corona on the disk is ∼50%, which indicates that half of the disk is covered by the corona. In this case, the disk corona model is preferred than the lamppost geometry of the corona.

From the burst light curves of LE and ME, the burst rises tend to have a convex shape, suggesting ignition near the equator (Maurer & Watts 2008). This scenario is somewhat incompatible with the hot spot near the poles. The inconsistency above may indicate another channel of accretion onto a magnetized NS, e.g., via Schwarzschild–Kruskal instability (the magnetic version of the Rayleigh–Taylor instability) (Arons & Lea 1976; Elsner & Lamb 1977) in the disk equatorial plane. This model proposes that several "tongues" of plasma penetrate the magnetosphere and impact the NS surface at random positions. This model has also been used to explain why bright LMXBs do not pulsate (Di Salvo 2022).

Bursting behavior is known to be extremely variable and violent, and the bursts influence the accretion process. To date, a significant soft excess is detected in most bright bursts, which is caused by the interaction between the burst and the corona and/or disk. However, in this work, this phenomenon is absent, or conservatively, not as significant as in other bursters. Accompanying the small fraction of the deficit in 30–100 keV, e.g., the deficit fraction of 4U 1636–536 (Ji et al. 2013; Chen et al. 2018) and Aql X–1 (Chen et al. 2013) is roughly unity, a larger inner-disk radius than other bursters is preferred, since the radiation pressure and the flux density of the burst imposed on the disk/corona is proportional to $1/R_{\rm disk}$. Other possibilities, such as MAXI J1816–195 that has different structures/physical parameters of the disk/corona than other bursters, cannot be ruled out. When more NICER data are available, more bursts from MAXI J1816–195 will be found to be simultaneously detected by NICER and Insight-HXMT. We expect to study those bursts in the forthcoming publication to better understand the interaction between the bursts and inferred outburst emission.

In the scenario that a burst cools the corona to a lower temperature, the fraction of the deficit should have a larger value in a higher energy band. For instance, assuming that the corona temperature is cooled by an amplitude of 10% during the bursts (from 10.8 to 9.7 keV), the count rates in 50–60 keV and 30–40 keV will be dropped by 50% and 30%, respectively. The above estimation is consistent with the results shown in Figure 5. We also notice that there is a clue that the fraction of the deficit drops at ∼65–85 keV. This may relate to another hard X-ray generator—the accretion column of the magnetic pole, which is not affected by the burst.

However, this trend is possibly not significantly detected because of the low count rate at >85 keV. It may also be the case that, at high energies, the hard X-rays are mostly from the accretion column of the magnetic pole rather than from the surrounding corona, which usually has a relatively lower temperature. Thus, dominant hard X-rays from the magnetic pole than from the corona could, in principle, contribute to such a decreasing deficit trend at higher energies. In this case, we predict that the pulsation fraction of hard X-rays should be higher than that of soft X-rays.

This work made use of the data and software from the Insight-HXMT mission, a project funded by China National Space Administration (CNSA) and the Chinese Academy of Sciences (CAS). This research has made use of data and software provided by data obtained from the High Energy Astrophysics Science Archive Research Center (HEASARC), provided by NASA's Goddard Space Flight Center. This work is supported by the National Key R&D Program of China (2021YFA0718500) and the National Natural Science Foundation of China under grants 11733009, U1838201, U1838202, U1938101, U2038101.

ORCID iDs

Yu-Peng Chen https://orcid.org/0000-0001-8768-3294
Shuang-Nan Zhang https://orcid.org/0000-0001-5586-1017
Peng-Ju Wang https://orcid.org/0000-0002-6454-9540
Ling-Da Kong https://orcid.org/0000-0003-3188-9079
Zhi Chang https://orcid.org/0000-0003-4856-2275
Jing-Qiang Peng https://orcid.org/0000-0002-5554-1088
Jian Li https://orcid.org/0000-0003-1720-9727
Lian Tao https://orcid.org/0000-0002-2705-4338
Ming-Yu Ge https://orcid.org/0000-0002-2749-6638
Jin-Lu Qu https://orcid.org/0000-0002-9796-2585

References

Arnaud, K. A. 1996, in ASP Conf. Ser. 101, Astronomical Data Analysis Software and Systems V., ed. G. H. Jacoby & J. Barnes (San Francisco, CA: ASP), 17
Arons, J, & Lea, S. M. 1976, ApJ, 207, 914
Ballantyne, D. R., & Strohmayer, T. E. 2004, ApJL, 602, L105
Beauchamp, I., Belvedere, S., Hernandez, M., et al. 2022, ATel, 15481
Bult, P., Altamirano, D., Arzoumanian, Z., et al. 2021, ApJ, 920, 59
Bult, P., Altamirano, D., Arzoumanian, Z., et al. 2022a, ApJL, 935, L32

Bult, P. M., Ng, M., Altamirano, W. I. D., et al. 2022b, ATel, 15425
Bult, P. M., Sanna, A., Ng, M., et al. 2022c, ATel, 15431
Burderi, L., Di Salvo, T., & Robba, N. R. 1998, ApJ, 498, 831
Chakrabarty, D., & Morgan, E. H. 1998, Natur, 394, 346
Chen, Y. P., Zhang, S., Qu, J. L., et al. 2018, ApJL, 864, 30
Chen, Y. P., Zhang, S., Torres, D. F., et al. 2011a, A&A, 510, 81
Chen, Y. P., Zhang, S., Zhang, S. N., et al. 2012b, ApJL, 752, 34
Chen, Y. P., Zhang, S., Zhang, S. N., et al. 2013, ApJL, 777, 9
Cumming, A. 2004, NuPhS, 132, 435
de Martino, D., D'Avanzo, P., Ambrosino, F., et al. 2022, ATel, 15479
Degenaar, N., Ballantyne, D. R., Belloni, T., et al. 2018, SSRv, 214, 15
Di Salvo, T. 2022, in Millisecond Pulsars, ed. B. Sudip, P. Alessandro, & B. Dipankar (Cham: Springer), 87
Elsner, R. F., & Lamb, F. K. 1977, ApJ, 215, 897
Galloway, D. K., In't Zand, J., Chenevez, J., et al. 2020, ApJS, 249, 32
Galloway, D. K., Muno, M. P., Hartman, J. M., et al. 2008, ApJS, 179, 360
Ghosh, P., & Lamb, F. K. 1978, ApJ, 223, 83
Güver, T., Bostanci, F., Boztepe, T., et al. 2022a, ApJ, 935, 154
Güver, T., Boztepe, T., Ballantyne, D. R., et al. 2022, MNRAS, 510, 1577
in't Zand, J. J. M., Galloway, D. K., Marshall, H. L., et al. 2013, A&A, 553, A83
Ji, L., Zhang, S., Chen, Y. P., et al. 2013, MNRAS, 432, 2773
Ji, L., Zhang, S., Chen, Y. P., et al. 2014a, ApJL, 791, L39
Ji, L., Zhang, S., Chen, Y. P., et al. 2014b, A&A, 564, A20
Kaastra, J. S., & Bleeker, J. A. M. 2016, A&A, 587, A151
Kajava, J. J. E., Koljonen, K. I. I., Nättilä, J., Suleimanov, V., & Poutanen, J. 2017, MNRAS, 472, 78
Kashyap, U., & Chakraborty, M. 2022, MNRAS, 512, 6180
Keek, L., Ballantyne, D. R., Kuulkers, E., & Strohmayer, T. E. 2014, ApJL, 797, L23
Kennea, J. A., Evans, P. A., & Negoro, H. 2022, ATel, 15467
Koljonen, K. I. I., Kajava, J. J. E., & Kuulkers, E. 2016, ApJ, 829, 91
Kuulkers, E., den Hartog, P. R., in 't Zand, J. J. M., et al. 2003, A&A, 399, 663
Lewin, W. H. G., van Paradijs, J., & Taam, R. E. 1993, SSRv, 62, 223
Li, X. B., Li, X. F., Tan, Y., et al. 2020, JHEAp, 27, 64
Maccarone, T. J., & Coppi, P. S. 2003, A&A, 399, 1151
Maurer, I., & Watts, A. L. 2008, MNRAS, 383, L387
Mestel, L. 1968, MNRAS, 138, 359
Negoro, H., Serino, M., & Iwakiri, W. 2022, ATel, 15425
Remillard, R. A., Loewenstein, M., Steiner, J. F., et al. 2022, AJ, 163, 130
Sánchez-Fernández, C., Kajava, J. J. E., Poutanen, J., et al. 2020, A&A, 634, A58
Strohmayer, T., & Bildsten, L. 2006, in Compact stellar X-ray Sources, ed. W. Lewin & M. van der Klis, Vol. 113 (Cambridge: Cambridge Univ. Press), 156
Wang, Y.-M. 1997, ApJL, 475, L135
Wijnands, R., & van der Klis, M. 1998, Natur, 394, 344
Wilms, J., Allen, A., & McCray, R. 2000, ApJ, 542, 914
Worpel, H., Galloway, D. K., & Price, D. J. 2013, ApJ, 772, 94
Worpel, H., Galloway, D. K., & Price, D. J. 2015, ApJ, 801, 60
Zdziarski, A. A., Szanecki, M., Poutanen, J., Gierlinski, M., & Biernacki, P. 2020, MNRAS, 492, 5234
Zhang, S.-N., Li, T.-P., Lu, F.-J., et al. 2020, SCPMA, 63, 249502
Zhao, G.-Y., Li, Z.-S., Pan, Y.-Y., et al. 2022, A&A, 660, A31